Journal of ELECTRONIC MATERIALS, Vol. 50, No. 1, 2021
https://doi.org/10.1007/s11664-020-08552-6

Enhanced Visible-Light Photocatalytic Activity and Mechanism of Ag@AgCl-Decorated TiO_2 Nanotubes

ZHENG ZHANG,[1] CHANGSHENG FENG,[1] CAIYUN JIANG,[2] and YUPING WANG[1,3]

1.—School of Chemistry and Material Science, Jiangsu Provincial Key Laboratory of Materials Cycling and Pollution Control, Nanjing Normal University, Nanjing 210023, China. 2.—Department of Engineering and Technology, Jiangsu Institute of Commerce, Nanjing 211168, China. 3.—e-mail: wangyuping@njnu.edu.cn

This paper describes the excellent photocatalytic and photoelectrochemical performance of Ag@AgCl/TiO_2 nanotubes (Ag@AgCl/TNTs) that were successfully prepared by a simple multistep reaction route. Using $AgNO_3$ as Ag source and HCl as Cl source, AgCl was loaded onto synthetic TNTs by a coprecipitation method, and some of the Ag^+ on the nanotubes was reduced to Ag^0 by a photoreduction method. The crystal structure, morphology, and properties of the materials were characterized by x-ray diffraction (XRD) analysis, transmission electron microscopy (TEM), Brunauer–Emmett–Teller (BET) measurements, x-ray photoelectron spectroscopy (XPS), ultraviolet–visible (UV–Vis) spectrophotometry, and photoluminescence (PL) techniques. The effects of using different ratios of Ag@AgCl on the photocatalytic performance of the composites were investigated via degradation of *o*-nitrobenzoic acid (*o*-NBA). The results showed that the optimum doping ratio of Ag@AgCl was 40%, and the removal rate of *o*-NBA by 40%Ag@AgCl/TNTs (40%AC/T) was 3.68 and 5.76 times higher compared with TNTs under visible light, respectively. When Ag@AgCl was loaded on TiO_2 nanotubes, the mechanism of activity enhancement of the prepared material can be regarded as the surface plasmon resonance (SPR) effect of Ag^0, which enhanced the response of the material to visible light, effectively achieving separation of photogenerated electrons and holes.

Key words: Ag@AgCl, TiO_2 nanotubes, heterojunction, nitrobenzoic acid, photocatalysis

INTRODUCTION

Photocatalytic oxidation has been demonstrated to be prominently superior for decomposition of pollutants that are toxic and difficult to treat using general biochemical methods.[1] Titanium dioxide (TiO_2), as one of the semiconductor materials with photocatalytic properties, had attracted widespread attention from researchers due to its advantages such as a suitable energy band potential, nontoxic and harmless nature, low cost, ready availability, good photoelectric conversion efficiency, and chemical stability.[2–4] However, titanium oxide can only be activated by light in the ultraviolet region, which accounts for only 3% to 5% of solar energy. In addition, photogenerated electrons and holes with slow transfer rates result in a low quantum efficiency for TiO_2. Compared with particles, titanium dioxide nanocrystalline spheres, titanium dioxide nanorods, and titanium dioxide nanotubes (TNTs) have a larger specific surface area and more active sites. Nevertheless, the use of titanium oxide with different morphologies as photocatalysts suffers from disadvantages such as low utilization of visible

(Received July 2, 2020; accepted October 7, 2020; published online October 30, 2020)
Zheng Zhang and Changsheng Feng contributed equally to this work.

light and high photogenerated electron–hole recombination rate.[5] To improve the photocatalytic activity of these materials under visible light, many studies have been carried out on titanium oxide with different morphologies.[6–8] Among them, Ag nanoparticles exhibit strong absorption of visible light due to the surface plasmon resonance (SPR) effect,[9] while Ag@AgCl catalyst is also highly efficient and stable under light. The heterojunction formed between Ag@AgCl and titanium oxide shows higher removal efficiency for organic materials.[10] W et al.[11] successfully prepared Ag@AgCl plasmonic photocatalyst via a hydrothermal–deposition–photoreduction method, and the removal efficiency of RhB reached 80.6% under irradiation for 2 h using this catalyst. In addition, the combination of Ag nanoparticles and AgCl improves the separation of photogenerated electrons and holes.[12] Recently, Ag/AgCl-modified titanium oxide (TiO_2) hollow spheres,[11] titanium oxide nanorods,[13,14] and titanium oxide nanoparticles[15] have been reported to show improved visible-light catalytic activity.

In this paper, we report that TiO_2 nanotubes decorated with Ag@AgCl show enhanced responsiveness to visible light. Ag@AgCl/TNTs composites were prepared by coprecipitation and photoreduction. First, AgCl was loaded onto TiO_2 nanotubes by a coprecipitation method, then Ag/AgCl/TNTs composite nanomaterials were prepared by photoreduction to reduce Ag^+ to Ag^0. *o*-Nitrobenzoic acid (*o*-NBA) was used as target pollutant, the photocatalytic activity of the composites was evaluated, and the effect of the amount of Ag@AgCl doping on the visible-light photocatalytic performance of the composites was investigated. Furthermore, the mechanism responsible for enhancing the visible-light catalytic activity was explored by free-radical trapping experiments and PL characterization.

EXPERIMENTAL PROCEDURES

Materials

Titanium oxide (P25) was purchased from Degussa. All chemicals and reagents were of analytical grade and used without further purification. Deionized (DI) water was prepared using a laboratory ultrapure water purifier.

Preparation of Photocatalysts

Preparation of TNTs

TiO_2 nanotubes were synthesized by a hydrothermal method.[16] Typically, 0.4 g TiO_2 was added to 10 mol/L NaOH solution (40 mL) and stirred continually for 30 min, then ultrasonically for 30 min. After mixing evenly, the solution was transferred to a 50-mL Teflon-lined stainless-steel autoclave and was treated at 150°C for 12 h. When the reaction was complete, the product was washed to neutral with DI water then immersed in 0.1 mol/L HCl for 24 h and washed to neutral with DI water. The precipitate was filtered and then dried in an oven at 80°C. Finally, the resulting white sample was calcined for 120 min at 400°C in air to obtain TNTs.

Preparation of Ag@AgCl-Modified TiO_2 Nanotubes (Ag@AgCl/TNTs)

Ag@AgCl nanoparticles were decorated on the prepared TNTs by continuous precipitation–photoreduction reaction. First, 0.1 g TNTs were dispersed in 40 mL water and subjected to ultrasound for 30 min. Then, a certain volume of $AgNO_3$ solution (0.1 M) was dropped into the solution under magnetic stirring, and stirring was continued for another 15 min. Subsequently, the same volume of HCl solution (0.1 M) was transferred to the above solution and stirred for 15 min. Finally, the mixture solution was exposed to a 300-W metal-halide lamp for 20 min to obtain Ag@AgCl/TNTs (*X*%AC/T for short). Samples containing $AgNO_3$ solution at different doses are denoted as 30%AC/T, 40%AC/T, and 50%AC/T, respectively. For comparison, a sample was prepared from P25 as raw material, being denoted as X%AC/P.

Characterization

The crystal structure of the as-obtained nanocomposites was characterized by powder x-ray diffraction (XRD) analysis (Rigaku D/max 2500VL/PC) using Cu K_α (λ = 1.5406 Å) radiation. The morphology and microstructure of the prepared products were observed by scanning electron microscopy (SEM, JSM-5610LV) and high-resolution transmission electron microscopy (HRTEM, JEOL JEM-2100). The specific surface area (S_{BET}) was analyzed by N_2 gas adsorption–desorption isotherm (ASAP-2000 Micromeritics Co., USA). The XPS spectrum (Thermo Fisher Ecsalab 250xi) was used to study the structure and components of each composite. The absorption spectrum of each photocatalyst was recorded in the wavelength range from 800 nm to 200 nm using an ultraviolet–visible (UV–Vis) spectrophotometer (Cary 5000) with $BaSO_4$ as reflectance standard to determine the bandgap . Photoluminescence (PL) measurements were carried out on a LS-50B fluorescence spectrophotometer at room temperature with an excitation wavelength of 280 nm.

Photocatalytic Experiments

The photocatalytic activity of the prepared composites was investigated by removing *o*-NBA from aqueous solution under visible light. Sunlight was simulated using a 350-W xenon lamp with a 400-nm cutoff filter to block ultraviolet light and leave visible light. An XPA-7 photochemical reactor (Nanjing Xujiang Electromechanical Plant, Nanjing, China) was employed for photodegradation experiments. Typically, 50 mg catalyst was added to 50 mL 50 mg/L *o*-NBA solution. Prior to diffraction

analysis, the above mixed solution was stirred in the dark for 30 min to achieve adsorption–desorption equilibrium between the catalyst and organic pollutant. In each experiment, about 5 mL suspension was taken out at regular intervals and centrifuged for 10 min. The relative concentration of *o*-NBA in solution was determined by high-performance liquid chromatography (HPLC). Firstly, the collected solution was filtered through a Millipore filter (0.45 μm), then the concentration of each sample was measured by HPLC. The degradation efficiency (D) after each experiment was calculated according to the formula

$$D = \frac{C_0 - C_t}{C_0} \times 100\%, \quad (1)$$

where C_t is the concentration of the pollutant at a certain sampling time t, and C_0 is the initial concentration of the pollutant. The mobile phase was water–methanol (35:65, v/v) with 1% acetic acid at a flow rate of 1 mL/min. A C-18 column (4.6 mm × 150 mm, 5 μm) was used at a temperature of 30°C. The sample volumes for injection were all 20 μL, and the detection wavelength was 267 nm.

Photoelectrochemical Experiments

Photoelectrochemical experiments were carried out using a CHI660E electrochemical workstation (Shanghai, CH Instruments, China) with a standard three-electrode cell. Indium tin oxide (ITO, 1 cm × 2 cm) glass plates were ultrasonically cleaned in acetone, alcohol, and DI water for 30 min, respectively. A suspension of the prepared sample (20 μL of 5 mg mL^{-1}) was obtained by ultrasonication in 0.1 wt.% chitosan solution (1 wt.% acetic acid) for 30 min, then dropped onto an ITO substrate to form the working electrode. A 350-W xenon lamp, Pt foil, and Ag/AgCl electrode (3 M) were used as the light source, and auxiliary and reference electrodes in the photoelectrochemical experiments, respectively. The photocurrent response curves of the different materials were studied at 0.1 M mol/L phosphate buffer solution (pH 7.4). The open-circuit potential (OCP) was measured in 0.1 M $NaSO_4$ solution. Electrochemical impedance spectroscopy (EIS) and cyclic voltammetry (CV) were performed in $Fe(CN)_6^{3-}/Fe(CN)_6^{4-}$ (5 mM) containing KCl solution (0.1 M). The electron lifetime was evaluated by plotting the Bode phase obtained by EIS under visible light.

RESULTS AND DISCUSSION

XRD Analysis

The XRD patterns of the as-obtained Ag@AgCl, TNTs, and composites are shown in Fig. 1. The pure TNTs had anatase phase structure without other diffraction peaks.[17] The five peaks characteristic of Ag@AgCl at 27.93°, 32.36°, 46.35°, 54.92°, and 57.5° in Joint Committee on Powder Diffraction Standards (JCPDS) card no. 31-1238 were assigned to (111), (200), (220), (311), and (222) crystal planes of cubic AgCl, respectively. A weak peak was observed at 2θ = 38.13°, corresponding perfectly to (111) planes of Ag in JCPDS card no. 04-0783.[18] The characteristic diffraction peaks of pure TNTs and pure Ag@AgCl were observed in the XRD patterns of the 40%AC/T and 40%AC/P catalysts, confirming successful preparation of the composites. The XRD patterns of the composites with different doping ratios are shown in Fig. 1b. With increasing Ag@AgCl doping amount, the diffraction peak of AgCl became more prominent, but the diffraction peak of Ag remained basically unchanged, probably due to the low content of Ag nanoparticles or low crystallinity.

TEM Analysis

The detailed microstructure of the prepared materials was clearly observed by TEM. The TEM image in Fig. 2a shows Ag@AgCl with irregular and near-spherical shape and average size of about 10 nm. As seen in Fig. 2b, TiO_2 nanotubes formed by curling were scattered randomly together, having an average size of 70 nm. Figure 2c reveals particulate matter on the TiO_2 nanotubes, indicating successful deposition of Ag@AgCl on their surface. These results indicate the formation of a heterojunction between the TNTs and Ag@AgCl nanoparticles, in agreement with the XRD results described above.

BET Analysis

Figure 3 showed the adsorption isotherms and pore size distribution of the TNTs and 40%AC/T. The results in Fig. 3a, b demonstrate that the adsorption–desorption isotherms of TNTs and 40%AC/T were of type IV, while the hysteresis loop in the curves indicates mesoporous structure.[19] Compared with the TNTs, the adsorption capacity of 40%AC/T was distinctly reduced while the hysteresis loop was significantly increased, which is related to the blockage of pores on the nanotubes by Ag@AgCl nanoparticles. As seen from Fig. 3c, d, the pore sizes of TNTs and 40%AC/T were mainly distributed around 30 nm and 15 nm, respectively. In addition to a narrow pore size distribution, the composite had fewer pores of the same size. The specific surface area and pore size parameters of TNTs and 40%AC/T were calculated according to the relevant formulae, and the results are shown in Fig. 3c, d. The specific surface area and pore volume parameters of 40%AC/T were reduced to some extent, which can be attributed to the fact that Ag@AgCl nanoparticles occupy part of the pores of the TNTs.

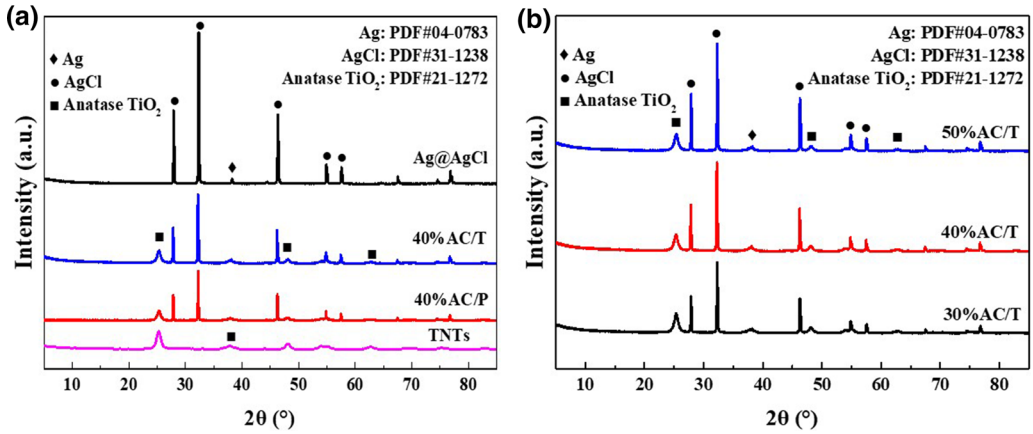

Fig. 1. XRD patterns of (a) ingredients and (b) composites with Ag@AgCl different doping ratios.

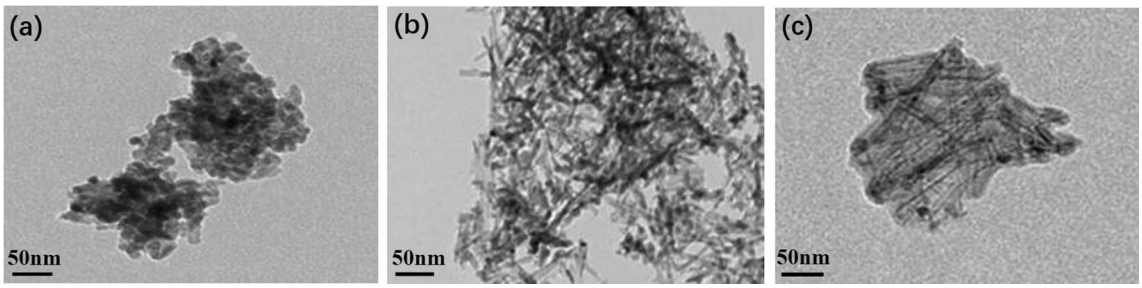

Fig. 2. TEM images of (a) Ag@AgCl, (b) TNTs, and (c) 40%AC/T.

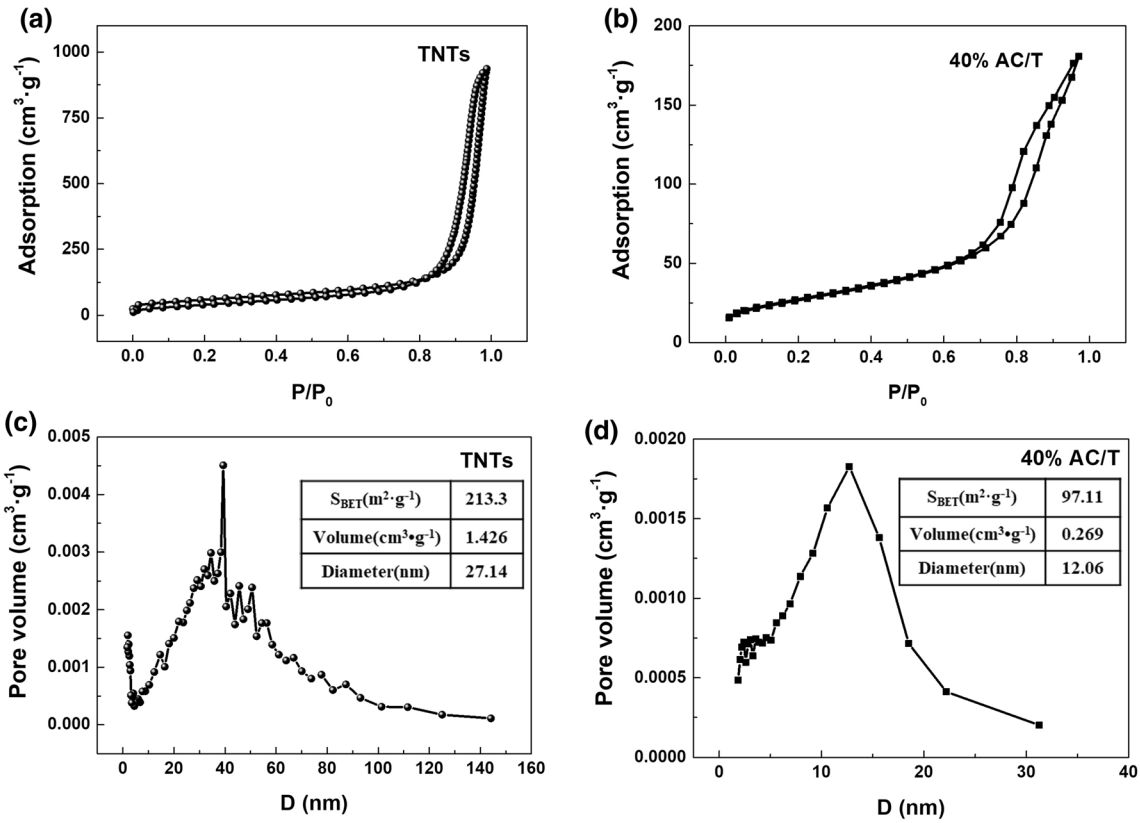

Fig. 3. N_2 adsorption–desorption isotherms of (a) TNTs and (b) 40%AC/T. Pore diameter of (c) TNTs and (d) 40%AC/T.

XPS Analysis

The XPS spectrum was measured to verify the chemical composition and states of the TNTs and 40%AC/T samples. The experimental results are shown in Fig. 4a, where the survey spectrum indicates that both TNTs and 40%AC/T samples contained Ti, O, and C elements, while the 40%AC/T sample also contained Ag and Cl elements. As shown in Fig. 4b, two peaks divided into 368.0 eV/368.9 eV and 374.0 eV/374.8 eV were observed for 40%AC/T, being assigned to Ag $3d_{5/2}$ and Ag $3d_{3/2}$. The peaks at 367.03 eV and 373.08 eV correspond to Ag^{+}, while the peaks at 366.68 eV and 372.53 eV indicate the presence of metallic Ag.[19] As seen in Fig. 4c, the Cl 2*p* peaks appearing at 197.33 eV and 198.85 eV were ascribed to Cl $2p_{3/2}$, and Cl $2p_{1/2}$, demonstrating that Cl was present as Cl^{-} ions on the surface of the sample.[20] These results prove that Ag and AgCl were successfully modified on the surface of the TNTs. Figure 4d compares the Ti 2*p* XPS results obtained from the surface of the TNTs and 40%AC/T samples, where the binding energies of about 458.87 eV and 464.2 eV can be respectively attributed to the Ti $2p_{3/2}$ and Ti $2p_{1/2}$ photoelectron peaks of Ti^{4+} in TNTs. An additional peak at 458.4 eV suggests incorporation of C in the local Ti–O bond structure.[21] By comparison, the characteristic Ti 2*p* XPS peaks showed a slight shift to lower binding energy after the chemical reduction, which can be attributed to electron transfer from the conduction band to oxygen vacancy state. The results also showed that after loading stable Ti^{4+} remained in the 40%AC/T sample.[22] Figure 4e shows high-resolution O 1*s* XPS spectra, where the characteristic peaks at O 1*s* can be fit by two peaks; the peaks at 531.33 eV and 531.37 eV are related to –OH in Ti–OH, while those at 529.57 eV and 529.78 eV are associated with the Ti–O bond in TiO_2. Compared with TNTs, the position of the O 1*s* binding energy peak of 40%AC/T shifted towards lower energy, and the adsorbed oxygen content also decreased slightly. As seen from Table I, the O/Ti atomic ratio in the TNTs and 40%AC/T samples was about 2.66:1 and 2.16:1, respectively, in agreement with the chemical composition of TiO_2. Besides, the sum of the weights of Ag and Cl elements was 10.12% of the sum of the weights of Ti and O elements, yielding a mass ratio of Ag@AgCl of 12.04%.

UV–Vis Diffuse Reflectance Spectra and PL Spectra

The UV–Vis absorbance spectrum shown in Fig. 5a was applied to study the optical properties of the TNTs, Ag@AgCl, and 40%AC/T samples. It was clear that the TNTs showed no obvious response to visible light, while Ag@AgCl showed a strong response in the visible range.[23] After Ag@AgCl was modified on the surface of the TNTs, 40%AC/T showed slightly enhanced absorption of light across the entire ultraviolet and visible region, which can be attributed to the SPR effect of the metallic Ag@AgCl nanoparticles (NPs) enhancing the response of TNTs to visible light and the TiO_2 nanotubes with larger active surface area dispersed with Ag@AgCl of different size. The bandgap of the photocatalyst was estimated using the formula

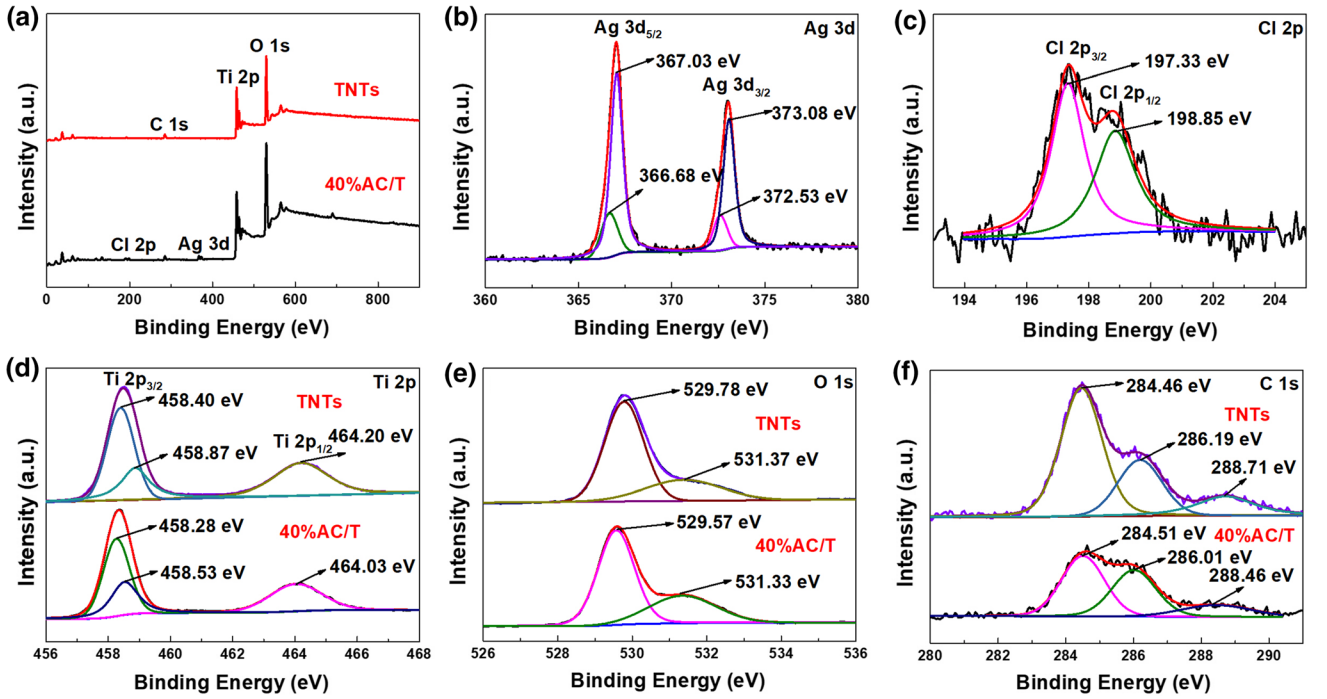

Fig. 4. XPS spectra: (a) survey spectrum, and (d) Ti 2*p*, (e) O 1*s*, (f) Cl 2*p* of TNTs, and (b) Ag 3*d* and (c) Cl 2*p* of 40%AC/T.

Table I. XPS results for chemical composition and relative content of each sample

Sample	Ti (%)	O (%)	C (%)	Ag (%)	Cl (%)
TNTs	24.78	65.88	9.34	—	—
40%AC/T	28.86	62.43	5.47	1.74	1.5

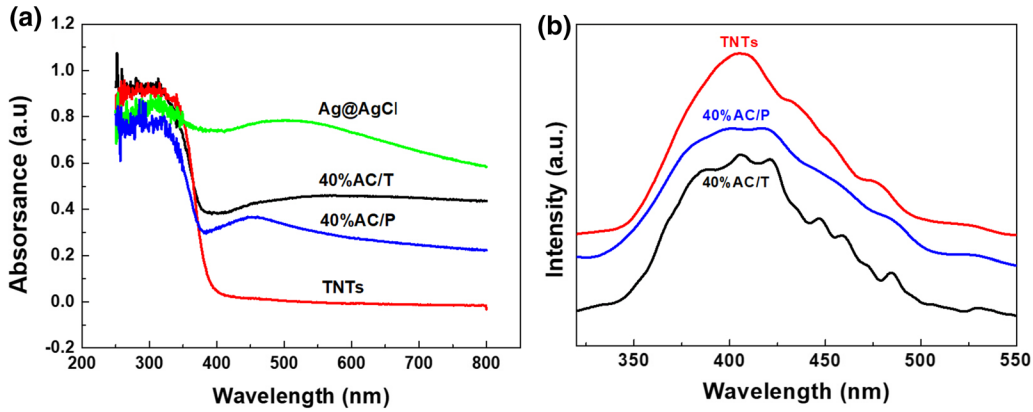

Fig. 5. (a) UV–Vis absorption spectra of Ag@AgCl, 40%AC/T, and TNTs. (b) PL spectra of TNTs and 40%AC/T.

$$E_g = 1240/\lambda_0, \quad (2)$$

where λ_0 is the absorption wavelength threshold obtained by the intercept method and E_g is the bandgap of the sample. According to this formula, the E_g value of the TNTs is calculated to be 3.2 eV.

PL can be used to analyze the capture, separation, and transfer of photogenerated electron–hole pairs on the photocatalyst surface. For photocatalysts, a lower PL intensity indicates a lower recombination rate of photogenerated electron–hole pairs but higher photocatalytic activity.[24] Figure 5b shows the PL spectra of the TNTs, 40%AC/T, and 40%AC/P samples obtained under an excitation wavelength of 320 nm. It can be seen that addition of Ag@AgCl caused an obvious reduction in the PL intensity, suggesting the highest separation efficiency of photogenerated electron–hole pairs. Studies have shown that higher separation efficiency is beneficial to improve the photocatalytic performance of a material.

Photoelectrochemical Study

It is generally accepted that the separation efficiency of electron–hole pairs has a significant effect on the photoelectrochemical conversion rate.[25] Several photoelectrochemical experiments were carried out to further study the transfer mechanism of electron–hole pairs. Figure 6a shows the photocurrent response of the TNTs and 40%AC/T electrodes under intermittent illumination. Compared with 40%AC/T, the pristine TNTs displayed weak photocurrent signals at 0 V under illumination. A higher photocurrent response indicates a higher separation rate of electron–hole pairs and photoelectric conversion ability.[26] The significant increment of the photocurrent values observed after the introduction of Ag@AgCl is due to the enhanced electrical conductivity and light absorption.[27] The OCP can be used to study the photoelectrochemical activity of the prepared materials. The potential value decreases sharply when the photogenerated electrons begin to accumulate under light irradiation.[28] As shown in Fig. 6b, the 40%AC/T sample displayed a more significant change in the potential value relative to TNTs, indicating that more electrons accumulated under light irradiation, indicating better separation of the photogenerated charges in 40%AC/T.[29]

The EIS electrochemical technique has been employed to investigate the rate of charge transfer on the surface of materials.[30] In general, the arc in the Nyquist diagram represents the charge transfer dynamics of the working electrode, while the diameter of the semicircle reflects the charge transfer resistance.[31] EIS was performed in (5 mM) $Fe(CN)_6^{3-}/Fe(CN)_6^{4-}$ containing KCl solution (0.1 M) in the frequency range from 0. 0.1 Hz to 10 kHz at 0.24 V. According to the results shown in Fig. 6c, electron transfer impedance (R_{et}) of the pure 40%AC/T sample was 103 Ω, being lower than the value of 210 Ω for the TNTs. These results indicate that addition of Ag@AgCl nanoparticles could accelerate the transfer of electrons. The lower R_{et} radius found for the 40%AC/T sample indicates more efficient separation of photogenerated electron–hole pairs, and a faster interface charge transfer rate.[32] Bode plots obtained from EIS measurements were applied to evaluate the electron lifetime under illumination based on the formula[33]

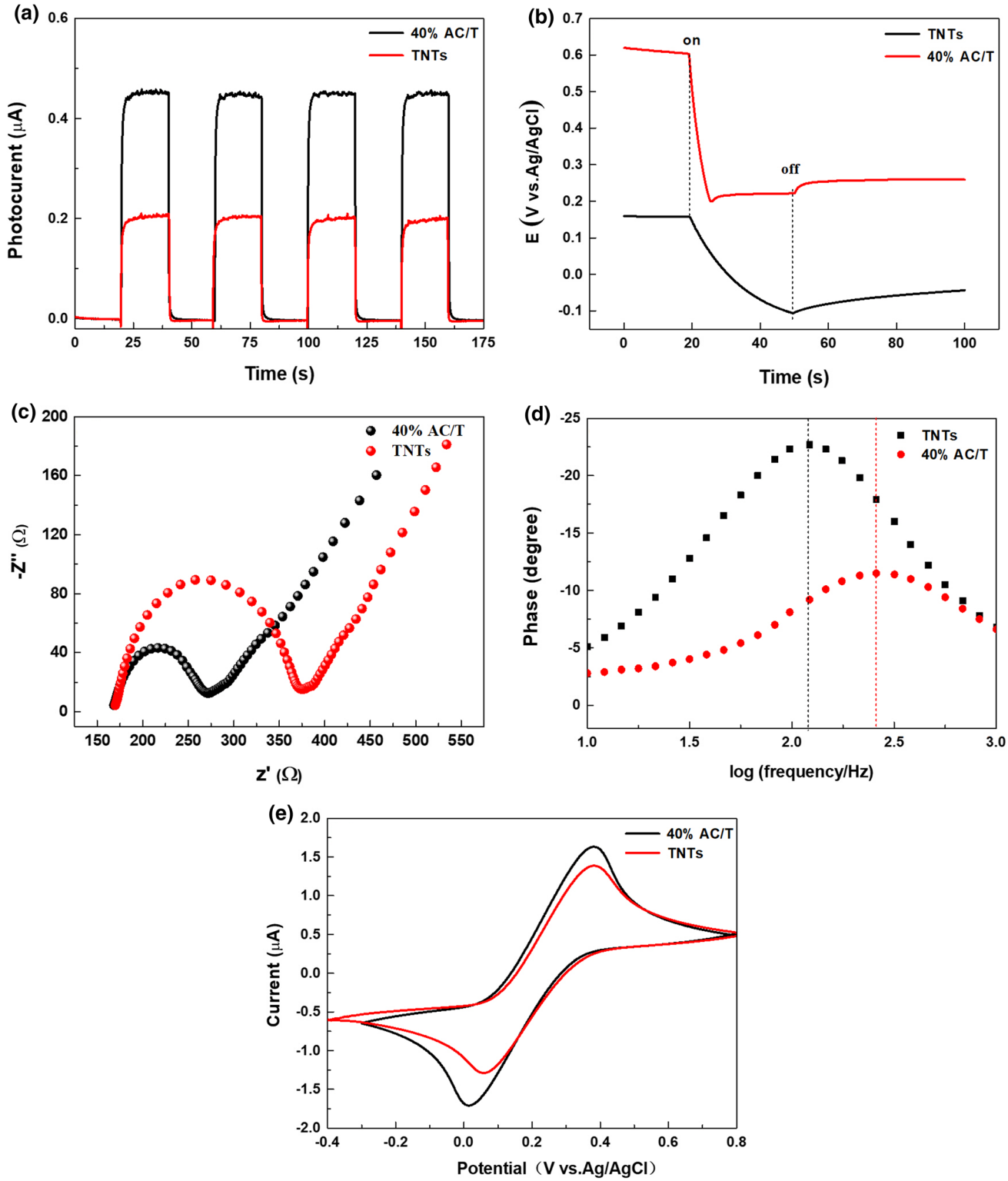

Fig. 6. (a) Photocurrent response curves, (b) OCP response curves, (c) EIS spectra, (d) Bode phase plots, and (e) CV spectra of TNTs and 40%AC/T.

$$\tau_e = 1/(2\pi f_{max}), \quad (3)$$

where τ_e is the electron lifetime and f_{max} is the peak frequency of the Bode phase plots. As can be seen from Fig. 6d, the Bode plot peak frequency of the TNTs and 40%AC/T samples was found to be 257 Hz, and 120 Hz, respectively, corresponding to τ_e values of 0.6 ms and 1.3 ms. The longer the electron lifetime of the photocatalysts, the higher

the charge separation efficiency.[34] More importantly, the results in the Bode phase plots are in accordance with the EIS and OCP results, confirming the superior photoelectrochemical properties of 40%AC/T. Figure 6e shows the CV curves of the TNTs and 40%AC/T recorded at a scan rate of 100 mV/s. Note that both the oxidation and reduction peak show a higher peak-to-current ratio for the TNTs than the 40%AC/T, confirming the good redox ability and electron transfer rate of the latter.[35]

Photocatalytic Performance

The photocatalytic performance of the obtained materials was evaluated by degradation of *o*-NBA under visible light. Figure 7a shows the degradation of *o*-NBA by different samples under visible light. The blank sample without any photocatalyst showed almost no degradation after a certain period of illumination, indicating that the photostability of *o*-NBA was good and the self-degradation of *o*-NBA was negligible. Compared with P25, the degradation rate of *o*-NBA was significantly improved when using the catalysts loaded with Ag@AgCl after 125 min of illumination; in particular, the degradation rate when using 40%AC/T reached almost 100%. These results clearly illustrate that all the samples loading with Ag@AgCl showed much better photocatalytic activity compared with TNTs or P25. Moreover, 40%AC/T showed higher photocatalytic efficiency compared with 30%AC/T or 50%AC/T, indicating the optimal Ag@AgCl doping amount. Once the amount of Ag@AgCl exceeds a critical value, it may cover some active sites on the surface of the TNTs, resulting in a reduction in the efficiency of photogenerated charge separation and transfer. For comparison, the identical mass of Ag@AgCl was deposited on both TiO_2 nanotubes and TiO_2 nanoparticles. It was found that the photocatalytic activity of the TiO_2 nanotubes was better compared with the nanoparticles. These results can be attributed to the higher specific surface area and stronger adsorption of the TiO_2 nanotubes. The first-order Langmuir–Hinshelwood kinetics was obtained from the degradation kinetic curve using the equation

$$-\ln(C/C_0) = Kt, \tag{4}$$

where C, C_0, and K are the concentration (mg/L) of the organic compound after illumination for time t, the concentration of the organic compound in equilibrium, and the rate constant (min^{-1}), respectively. As shown in Fig. 7b, $-\ln(C/C_0)$ of the different samples matched a good linear relationship with

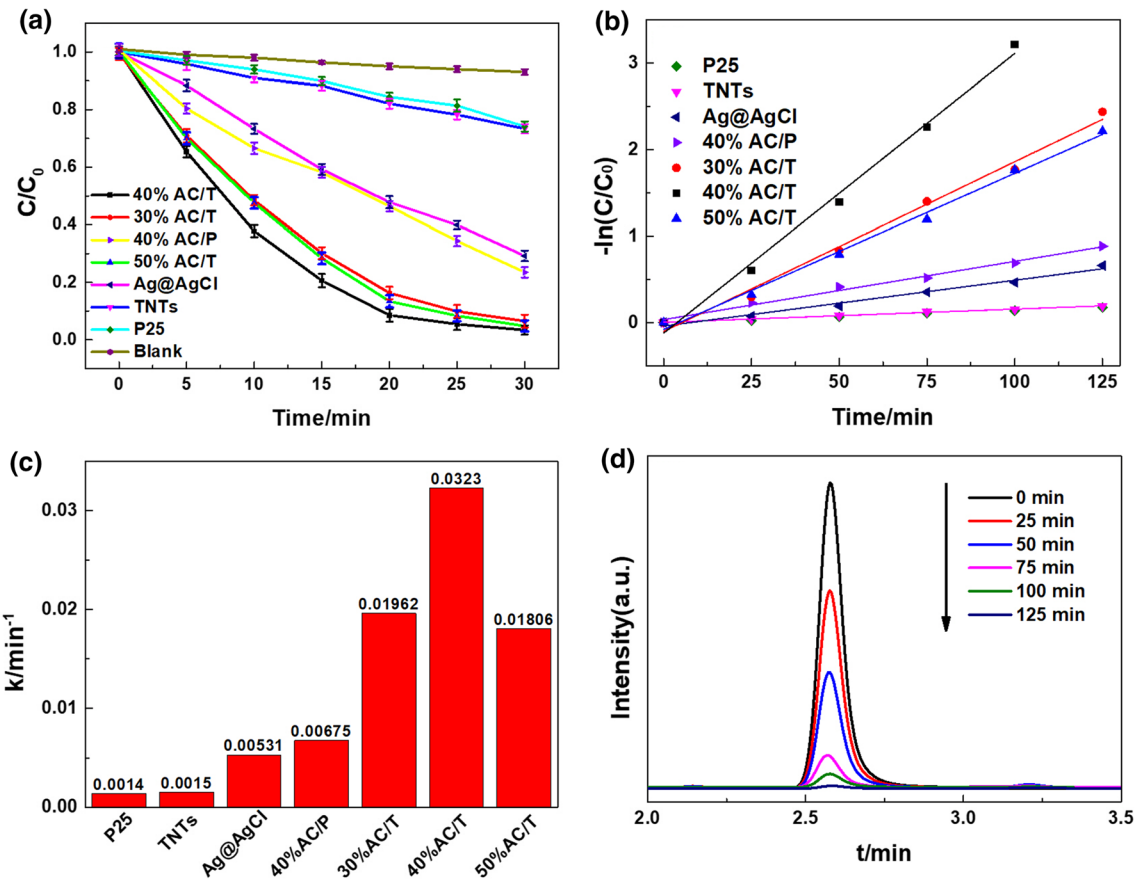

Fig. 7. (a) Photocatalytic degradation of *o*-NBA by all samples under visible-light irradiation, (b) kinetic fit for *o*-NBA degradation, (c) the corresponding reaction rate constant *k* for all the samples, and (d) liquid chromatogram of *o*-NBA for all the samples.

time t, indicating that the photodegradation process of the pollutant follows a pseudo-first-order model well. The rate constants (k) of the as-prepared samples are shown in Fig. 7c, where it can be observed that 40%AC/T exhibited the highest degradation rate for *o*-NBA compared with TNTs. The degradation rate of *o*-NBA was 21.53 times that of TNTs. The variation of the liquid chromatographic peak of *o*-NBA degraded by 40%AC/T photocatalysts is shown in Fig. 7d. As the illumination time was prolonged, the chromatographic peak of *o*-NBA at a retention time of 2.57 min gradually disappeared into a straight line within 125 min, indicating that the *o*-NBA was almost completely degraded. To further evaluate the photocatalytic activity of the prepared materials, the degradation effect on rhodamine B (RhB) as a target pollutant is presented in Supplementary Fig. S1.

Experiments to investigate the effect of the initial concentration of *o*-NBA solution and 40%AC/T dose on the degradation effect were also carried out using 10, 20, 30, 40, and 50 mg/L *o*-NBA solutions and 0.5, 1.0, 1.5, 2.0, and 2.5 g/L 40%AC/T doses. Figure 8a, b shows that the degradation efficiency and pseudo-first-order rate k decrease with increasing *o*-NBA concentration. It can be seen that the degradation efficiency for the different initial concentrations of *o*-NBA by 40%AC/T is in agreement with pseudo-first-order kinetics, and the degradation rate constant k reaches a maximum at 15 mg/L, being 2.75 times higher than that at 30 mg/L. The degradation efficiency and reaction kinetics of the *o*-NBA photodegradation at different 40%AC/T doses are shown in Fig. 8c, d. As the concentration was increased to 15 mg/L, 20 mg/L, 25 mg/L, and 30 mg/L, the removal rate of *o*-NBA increased from 95.52% to 100% after reaction for 125 min. The pseudo-first-order kinetics can better describe the photocatalytic degradation of *o*-NBA at different 40%AC/T doses. The optimal reaction rate constant k was obtained when the concentration of the catalyst was 1 g/L.

To verify whether the as-prepared sample completely degraded *o*-NBA, the total organic carbon (TOC) and NO^{3-} content in the solution before and after degradation were determined. It can be seen from Fig. 9a that, after 125 min of visible-light irradiation, the TOC removal rates of TNTs, P25, and 40%AC/T from 15 mg/L *o*-NBA were 8.03%, 11.21%, and 70.3%, respectively. The TOC removal rate of *o*-NBA solution was the highest with 40%AC/T catalyst, which is consistent with the results of the photocatalytic experiments. The removal rate of TOC using 40%AC/T was 8.75 times that when

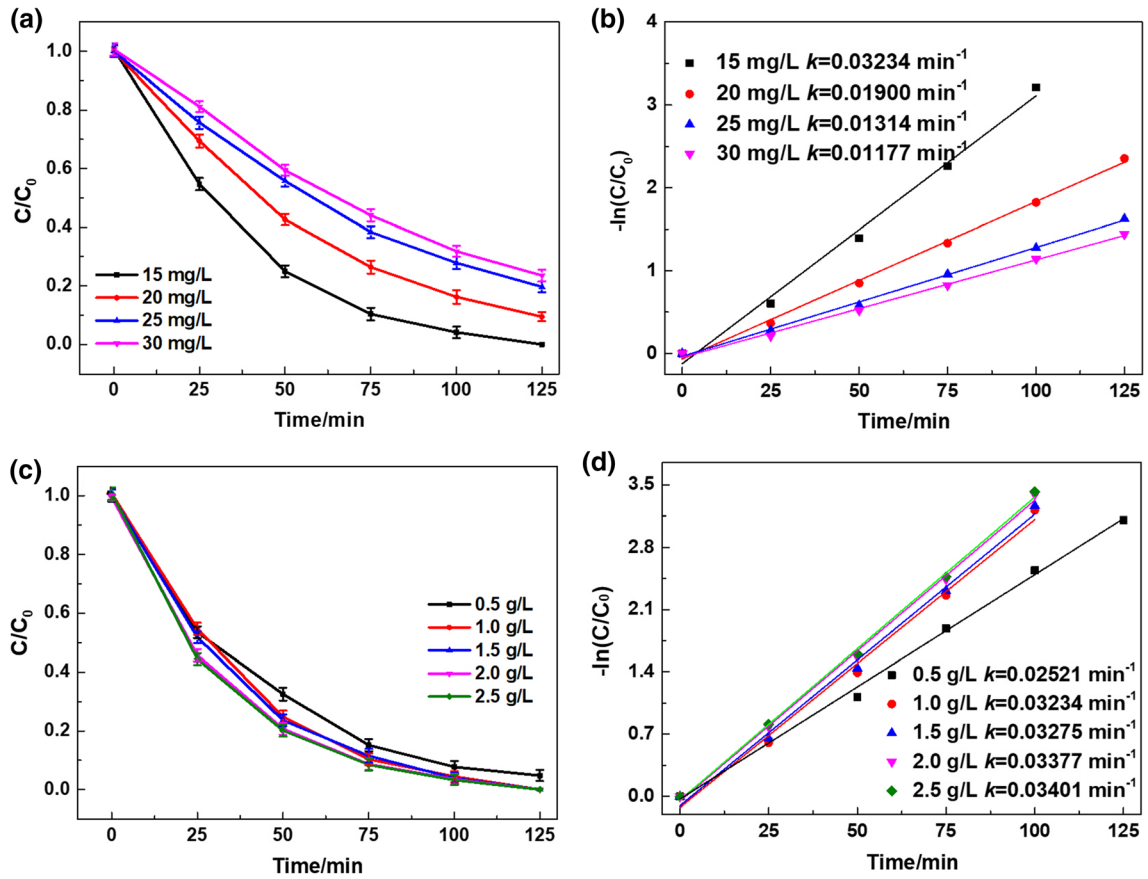

Fig. 8. Effect of (a) *o*-NBA concentration on its degradation and (b) the kinetic study. Effect of (c) catalyst dose on *o*-NBA degradation and (d) kinetic study.

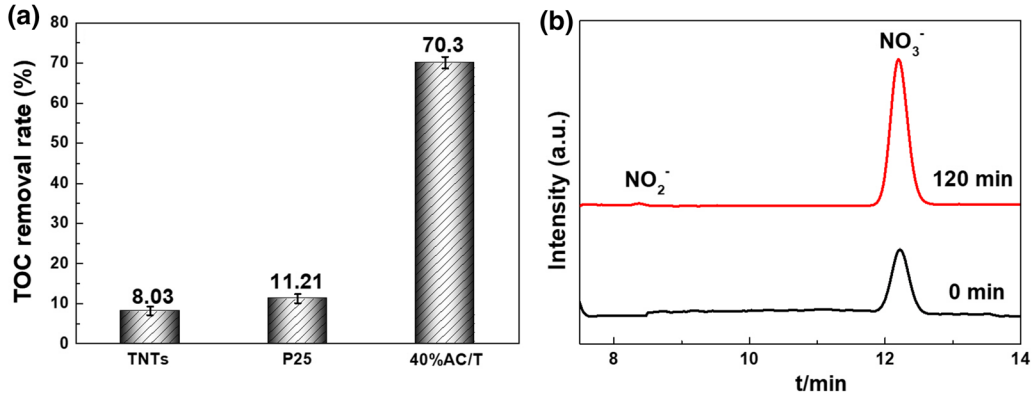

Fig. 9. (a) TOC removal rate of *o*-NBA solution using different catalysts. (b) Nitrate ion content in *o*-NBA solution before and after degradation.

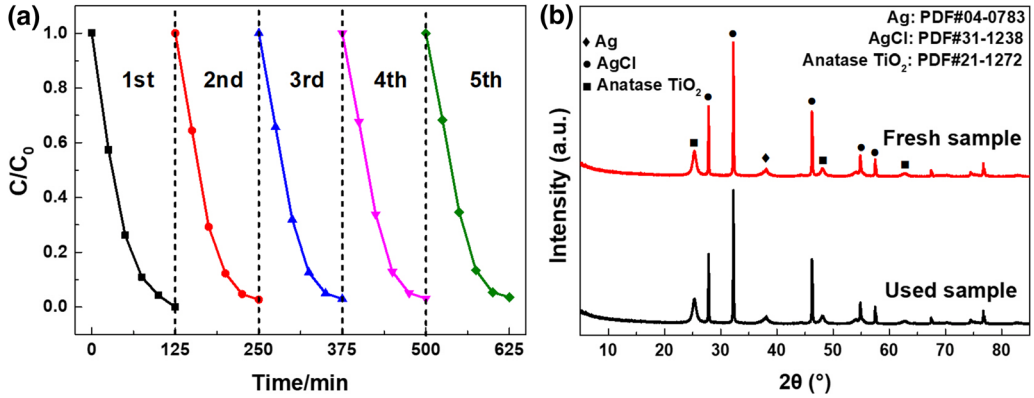

Fig. 10. (a) Cycling degradation of *o*-NBA under visible-light irradiation over 40%AC/T. (b) XRD patterns of 40%AC/T under visible-light irradiation.

using TNTs and 6.27 times that when using P25. As shown in Fig. 9b, the photodegradation of 15 mg/L *o*-NBA solution by 40%AC/T catalyst revealed that the NO^{3-} concentration in the solution increased significantly and the concentration of NO^{2-} increased slightly after 125 min. The concentration of NO_3^- in the solution increased from 2.74 mg/L to 6.10 mg/L according to the fitting formula for nitrate ions. These results show that NO^{2-} in the *o*-NBA is broken under visible-light irradiation and oxidized to the more stable NO^{3-}. The rate of increase of total N was calculated to be 60.38% after deducting N in water, being basically consistent with the degradation removal rate of *o*-NBA.

The stability of photocatalysts is also important for their practical applications. The stability of the 40%AC/T photocatalyst was investigated under visible light for degradation of *o*-NBA (Fig. 10a). The results showed that the photocatalytic effect of the prepared 40%AC/T did not change significantly over five cycles of photodegradation of *o*-NBA, indicating that the composite has superior photocatalytic stability and can be recycled many times. The stability of 40%AC/T was also examined by XRD analysis (Fig. 10b). Comparing the patterns obtained before and after the reaction, the XRD spectra of the catalyst after repeated recycling remained basically consistent with that of the original catalyst. All the results described above illustrate that the composite material showed high lattice stability and good prospects for application in actual treatment of wastewater.

Possible Photocatalytic Mechanism

Generally speaking, electrons (e^-), holes (h^+), superoxide ion radicals ($\cdot O_2^-$), and hydroxyl radicals ($\cdot OH$) play a certain role as active species in photodegradation processes. To explore the main photocatalytic mechanism of the reaction, $AgNO_3$, Ammonium oxalate (AO) *p*-benzoquinone (BQ), and *tert*-butanol (TBA) were added as scavengers of e^-, h^+,$\cdot O_2^-$, and $\cdot OH$ radicals. Figure 11 shows that the degradation efficiency of RhB after addition of $AgNO_3$, TBA, AO, and BQ was 99.93%, 98.92%, 70.71%, and 62.61%, respectively. The degradation

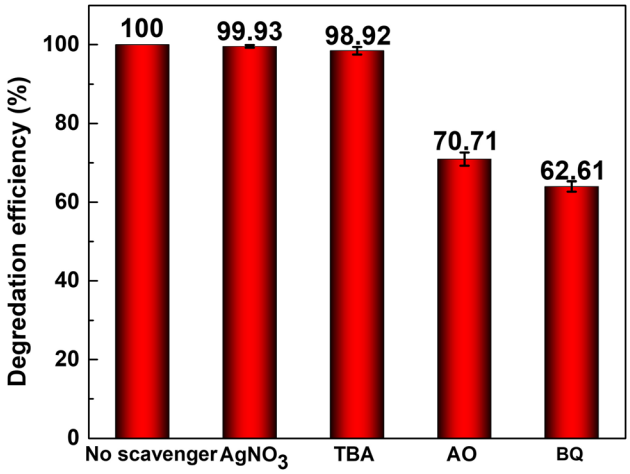

Fig. 11. Degradation rate of RhB with 40%AC/T catalyst in presence of various trapping agents.

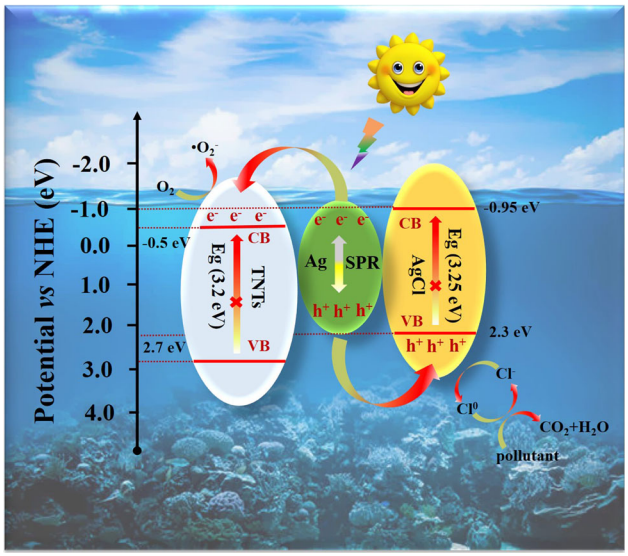

Fig. 12. Schematic of charge separation and transfer in 40%AC/T photocatalyst under visible-light irradiation.

efficiency was affected by the scavengers in the following order: $e^- < \cdot OH < h^+ < +\cdot O_2^-$. Therefore, $\cdot O_2^-$ and h^+ are the dominant active species, whereas e^- and ·OH play an auxiliary role in the photodegradation process.

Given the analysis above, a possible photodegradation enhancement mechanism of 40%AC/T composite can be proposed as shown in Fig. 12. With reference to related reports, the bandgap of TiO_2 nanotubes and AgCl was calculated to be 3.2 eV and 3.25 eV, respectively.[36] Due to the high bandgap, TNTs and AgCl cannot be easily excited under visible-light irradiation. Ag nanoparticles can successfully separate absorbed photons into electrons and holes due to the strong SPR effect. These Ag nanoparticles produce photogenerated electrons with energy in the range from 1.0 eV to 4.0 eV, making it easy to overcome the Schottky barrier for transfer to the surface of the TNTs.[37,38] After that, the electrons were captured by dissolved oxygen in the water to form $\cdot O_2^-$, which appear as the main reactive active component on the surface of the 40%AC/T photocatalyst. The continuously formed superoxide radicals can efficiently oxidize pollutants and achieve high degradation rates. Simultaneously, some of the holes on Ag nanoparticles could migrate to the surface of AgCl and react with Cl^-, which would produce Cl^0 atoms with excellent oxidation capability. The Cl^0 atom can effectively oxidize organic compounds and self-reduce to Cl^- again.[39] The residual holes in the valence band (VB) of AgCl could be trapped by OH^- to form ·OH, accelerating the breakdown of pollutants to carbon dioxide and water. Therefore, the modification of Ag@AgCl reduces the driving threshold of visible light and produces Cl^0 with strong oxidizing ability, effectively improving the photocatalytic activity of the 40%AC/T photocatalyst.

CONCLUSIONS

Composite 40%AC/T based on TNTs were successfully constructed by depositing AgCl NPs on TNTs followed by photoreduction of some Ag^+ ions of the AgCl nanoparticles to Ag^0. The crystal phase, composition, and morphology of the as-prepared sample were characterized by XRD analysis, TEM, XPS, UV–Vis, PL, and BET analysis. The photocatalytic activity of the 40%AC/T catalyst was investigated by degradation of RhB and *o*-NBA solutions. The degradation rate of 10 mg/L RhB by 40%AC/T was 96.55% within 30 min, while the degradation rate of 15 mg/L *o*-NBA solution by 40%AC/T photocatalyst could reach 100% within 125 min even after five cycles of reaction. These results illustrate that the 40%AC/T composite possesses strong visible-light absorption capability and low recombination efficiency of photoelectron-hole pairs due to the dispersion of Ag@AgCl. In addition, the 40%AC/T composites exhibited high photocatalytic activity, which could be completely attributed to the SPR effect of the Ag NPs and the formation of heterojunctions between Ag, AgCl, and TNTs.

ACKNOWLEDGMENTS

This study was supported by the National Natural Science Foundation of China (Grant 51578295), National Natural Science Foundation of Jiangsu Province (BK20161479), and Jiangsu Key Laboratory of Chemical Pollution Control and Resources Reuse (Nanjing University of Science and Technology), Qing Lan Project of Jiangsu Province. Additionally, we also appreciate the Foundation of Jiangsu Collaborative Innovation Center of Biomedical Functional Materials and a project funded by the priority academic program development of Jiangsu Higher Education Institutions.

CONFLICT OF INTEREST

The authors declare no conflicts of interest associated with this manuscript.

ELECTRONIC SUPPLEMENTARY MATERIAL

The online version of this article (https://doi.org/10.1007/s11664-020-08552-6) contains supplementary material, which is available to authorized users.

REFERENCES

1. S.Q. Song, A.Y. Meng, S.J. Jiang, B. Cheng, and C.J. Jiang, *Appl. Surf. Sci.* 396, 1368 (2017).
2. S. Banerjee, S.K. Mohapatra, P.P. Das, and M. Misra, *Chem. Mater.* 20, 6784 (2008).
3. J.C. Xu, M. Lu, X.Y. Guo, and L.L. Hu, *J. Mol. Catal. A* 226, 123 (2005).
4. T.A. Saleh and V.K. Gupta, *J. Colloid Interface Sci.* 371, 101 (2012).
5. H.L. Hoşgün and M.T.A. Aydın, *J. Mol. Struct.* 1180, 676 (2019).
6. M.H. Razali, A.F.M. Noor, and M. Yusoff, *Sci. Adv. Mater.* 9, 1032 (2017).
7. J. Fei and J. Li, *Adv. Mater.* 27, 31 (2015).
8. M. Vanitha, Keerthi, S. Vadivel, and N. Balasubramanian, *Desalin. Water. Treat* 54, 2748 (2015).
9. J. Ge, Y. Chen, J. Xu, Y.J. Liu, L. Zhang, and F.G. Zha, *Aust. J. Chem.* 72, 200 (2019).
10. Y.H. Ao, J.Q. Bao, P.F. Wang, and C. Wang, *J. Alloys Compd.* 698, 410 (2017).
11. H.Y. Yin, X.L. Wang, L. Wang, L. Wang, Q. Nie, Y. Zhang, Q.L. Yuan, and W.W. Wu, *J. Alloys Compd.* 657, 44 (2016).
12. G.G. Bondarenko, V.S. Petrov, and A.A. Komkova, *Catal. Today* 240, 100 (2015).
13. X.Z. Liang, P. Wang, M.M. Li, Q.Q. Zhang, Z.Y. Wang, Y. Dai, X.Y. Zhang, Y.Y. Liu, M. Whangbo, and B.B. Huang, *Appl. Catal. B* 220, 356 (2018).
14. Y.F. Wang, M. Zhang, J. Li, H.C. Yang, J. Gao, G. He, and Z.Q. Sun, *Appl. Surf. Sci.* 476, 84 (2019).
15. Q.L. Yang, M.Y. Hu, J. Guo, Z.H. Ge, and J. Feng, *J. Materiomics* 4, 402 (2018).
16. Z. Zhang, J.K. Jia, C.Y. Jiang, W.X. Huang, C.S. Feng, and Y.P. Wang, *J. Nanjing Normal Univ. (Nat. Sci Ed.)* 41, 52 (2018).
17. Y. Chen, D.W. He, Y.S. Wang, and B.Y. Yang, *Chin. J. Lumin.* 40, 177 (2019).
18. J. Wen, C.G. Niu, D.W. Huang, L. Zhang, C. Liang, and G.M. Zeng, *J. Catal.* 355, 73 (2017).
19. X. Yao, M.G. Li, Y.C. Xie, F. Liu, Q. Liu, Y. Liu, P. Li, R.T. Xue, and X.M. Fan, *Chin. J. Inorg. Chem.* 34, 1086 (2018).
20. X.M. Sun and L.J. Gao, *Acta. Phys. Chim. Sin.* 31, 1521 (2015).
21. S. Anandan, T. Narasinga Rao, M. Sathish, D. Rangappa, I. Honma, and M. Miyauchi, *ACS Appl. Mater. Interfaces* 5, 207 (2012).
22. P. Liziê, L. Bach-Toledo, J. Schultz, A.S. Mangrich, and P.G. Peralta-Zamora, *J. Braz. Chem. Soc.* 6, 31 (2020).
23. H. Li, Y. Tian, Z.F. Deng, and Y. Liang, *Analyst* 137, 4605 (2012).
24. M.C. Zhang, C. Tian, L.Y. Dang, S.F. Zhao, and Q.S. Lu, *Mater. Lett.* 207, 8 (2017).
25. K. Qian, L. Xia, W. Wei, L.L. Chen, Z.F. Jiang, J.J. Jing, and J.M. Jing, *Mater. Lett.* 206, 245 (2017).
26. J. Jiang, X. Zhang, P.B. Sun, and L.Z. Zhang, *J. Phys. Chem. C* 115, 20555 (2011).
27. Q.J. Xiang, J.G. Yu, and M. Jaroniec, *J. Phys. Chem. C* 115, 7355 (2011).
28. K. Yan, Y. Liu, Y.H. Yang, and J.D. Zhang, *Anal. Chem.* 87, 12215 (2015).
29. H. Dai, S.P. Zhang, Z.S. Hong, and Y.Y. Lin, *Anal. Chem.* 88, 9532 (2016).
30. Y.W. Hu, F.H. Li, D.H. Han, T.S. Wu, Q.X. Zhang, L. Niu, and Y. Bao, *Anal. Chim. Acta* 753, 82 (2012).
31. X.J. Du, D. Jiang, L.M. Dai, L. Zhou, N. Hao, J. Qian, B.J. Qiu, and K. Wang, *Biosens. Bioelectron.* 81, 242 (2016).
32. Q. Lu, X.M. Chen, L. Nie, J. Luo, H.J. Jiang, L. Chen, Q. Hu, S.H. Du, and Z.P. Zhang, *Talanta* 81, 959 (2010).
33. S.F. Hung, F.X. Hung, Y.Y. Hung, N.T. Suen, H.B. Yang, H.M. Chen, and B. Liu, *Adv. Energy. Mater.* 6, 1501339 (2016).
34. M.D. Ye, D.J. Zheng, M.Q. Lv, C. Chen, C.J. Lin, and Z.Q. Lin, *Adv. Mater.* 25, 3039 (2013).
35. H. Ming, H.C. Zhang, Z. Ma, H. Huang, S.Y. Lian, Y. Wei, Y. Liu, and Z.H. Kang, *Appl. Surf. Sci.* 258, 3846 (2012).
36. X.X. Yao and X.H. Liu, *J. Mol. Catal. A* 393, 30 (2014).
37. L.G. Devi and R. Kavitha, *Appl. Surf. Sci.* 360, 601 (2016).
38. Y.C. Yao, X.R. Dai, X.Y. Hu, S.Z. Huang, and Z. Jin, *Appl. Surf. Sci.* 387, 469 (2016).
39. W. Gan, X.C. Fu, and J. Zhang, *Mater. Sci. Eng. B* 229, 44 (2018).